

Enhancing the Selectivity and Transparency of the Electron Contact in Silicon Heterojunction Solar Cells by Phosphorus Catalytic Doping

Weiyuan Duan,* Gilbert Mains, Habtamu Tsegaye Gebrewold, Karsten Bittkau, Andreas Lambertz, Binbin Xu, Volker Lauterbach, Alexander Eberst, Nathan Nicholson, Lars Korte, Muhammad Ainul Yaqin, Kai Zhang, Qing Yang, Uwe Rau, and Kaining Ding*

An intrinsic hydrogenated amorphous silicon (a-Si:H(i)) film and a doped silicon film are usually combined in the heterojunction contacts of silicon heterojunction (SHJ) solar cells. In this work, a post-doping process called catalytic doping (Cat-doping) on a-Si:H(i) is performed on the electron selective side of SHJ solar cells, which enables a device architecture that eliminates the additional deposition of the doped silicon layer. Thus, a single phosphorus Cat-doping layer combines the functions of two other layers by enabling excellent interface passivation and high carrier selectivity. The overall thinner layer on the window side results in higher spectral response at short wavelengths, leading to an improved short-circuit current density of 40.31 mA cm^{-2} and an efficiency of 23.65% (certified). The cell efficiency is currently limited by sputter damage from the subsequent transparent conductive oxide fabrication and low carrier activation in the a-Si:H(i) with Cat-doping. Numerical device simulations show that the a-Si:H(i) with Cat-doping can provide sufficient field effect passivation even at lower active carrier concentrations compared to the as-deposited doped layer, due to the lower defect density.

solar capacity exceeds 1 TW and has to grow even faster.^[2] The majority of PV systems have used silicon solar cells since 1970 and are now the cheapest source of electricity among all others.^[3] One way to further reduce the overall cost of the PV power generation system, known as the Levelized Cost of Electricity (LCOE), is to improve the conversion efficiency of silicon solar cells. Silicon heterojunction (SHJ) solar cells represent a promising technological approach for higher PV efficiencies and lower fabrication cost, which is considered as a good candidate for next-generation mainstream products. SHJ solar cells can be fully processed at low temperatures and with lean processes. In recent years, SHJ technology has successfully developed and increased the world record for silicon solar cell conversion efficiency to over 26.81%.^[4] This has demonstrated the advantage of this technology and generated interest in both academy and industry to further improve the efficiency of the solar cells.

In SHJ solar cells, stacks of intrinsic hydrogenated amorphous silicon (a-Si:H(i)) and phosphorus or boron doped hydrogenated amorphous silicon (a-Si:H(n/p)) layers are used on both sides of the crystalline silicon wafer (c-Si), providing excellent passivation

1. Introduction

Global photovoltaic (PV) installation is increasing every year and has reached 228.5 GW in 2022,^[1] while the cumulative installed

W. Duan, G. Mains, H. T. Gebrewold, K. Bittkau, A. Lambertz, B. Xu, V. Lauterbach, A. Eberst, M. A. Yaqin, K. Zhang, Q. Yang, U. Rau, K. Ding
IEK-5 Photovoltaik
Forschungszentrum Jülich GmbH
52428 Jülich, Germany
E-mail: w.duan@fz-juelich.de; k.ding@fz-juelich.de

G. Mains, H. T. Gebrewold, B. Xu, A. Eberst, M. A. Yaqin, K. Zhang, Q. Yang, U. Rau
JARA Energy and Faculty of Electrical Engineering and Information Technology
RWTH Aachen University
52074 Aachen, Germany
N. Nicholson, L. Korte
Helmholtz-Zentrum Berlin für Materialien und Energie GmbH
Institute Silicon Photovoltaics
12489 Berlin, Germany

The ORCID identification number(s) for the author(s) of this article can be found under <https://doi.org/10.1002/adfm.202310552>

© 2023 The Authors. Advanced Functional Materials published by Wiley-VCH GmbH. This is an open access article under the terms of the Creative Commons Attribution-NonCommercial-NoDerivs License, which permits use and distribution in any medium, provided the original work is properly cited, the use is non-commercial and no modifications or adaptations are made.

DOI: 10.1002/adfm.202310552

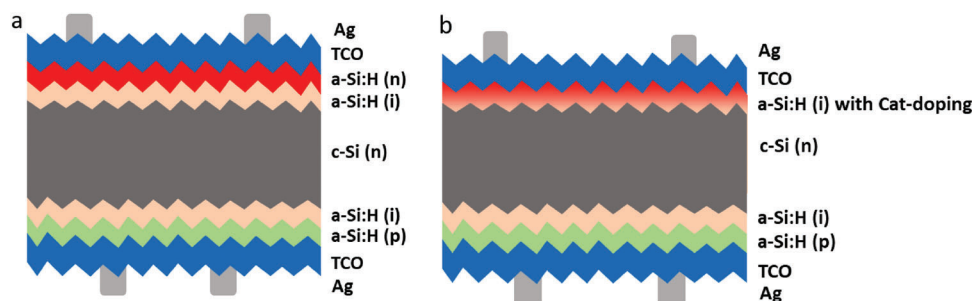


Figure 1. a) Sketch of a traditional SHJ solar cell using a-Si:H(i)/a-Si:H(n) stack on the window side. b) Sketch of a SHJ solar cell using a-Si:H(i) with Cat-doping on the window side, the as-deposited a-Si:H(n) is omitted. The two cell structures have the same rear configuration.

quality and charge carrier selectivity.^[5–7] Initially, heterojunction solar cells with a structure of doped a-Si:H deposited directly on c-Si wafer were investigated but yielded relatively low open-circuit voltage (V_{OC}) and fill factor (FF).^[8–11] Substitutional doping of a-Si:H leads to the formation of energetically deep defect states in the bulk of a-Si:H.^[12] but also at or near the a-Si:H/c-Si interface. This high number of defects leads to high recombination rates and reverse leakage currents at the a-Si:H/c-Si heterointerface. A turning point in SHJ technology was reached when researchers at Sanyo inserted a few nm thin a-Si:H(i) layer between the doped a-Si:H and the crystalline Si wafer.^[13] The a-Si:H(i) (passivation) layer has a low defect concentration and a high hydrogen concentration,^[14] effectively saturating the silicon dangling bonds and thus achieving good chemical passivation of the critical interface.^[15] Since then, this bilayer structure (as shown in **Figure 1a**) has become the state-of-the-art enabling the success story of SHJ and becoming one of the most efficient and industrially relevant types of wafer-based silicon solar cells.

However, the parasitic light absorption in the short-wavelength range of the solar spectrum by the bilayer stack reduces the short-circuit current density (J_{SC}) in SHJ solar cells and is considered as an important efficiency-limiting factor of this solar cell technology.^[16–18] Therefore, numerous studies have focused on replacing the highly absorbing a-Si:H layers with wider bandgap materials such as hydrogenated nanocrystalline silicon oxide (nc-SiO_x:H)^[19–21] or hydrogenated nanocrystalline silicon carbide (nc-SiC:H).^[22,23] In contrast, the present paper demonstrates that this J_{SC} limitation can be tackled by using a single undoped a-Si:H(i) passivation layer and replacing the doped silicon thin film layer with phosphorus catalytic doping (Cat-doping) of the undoped layer. In this way, the three functions of the bilayer stack, the chemical surface passivation by the undoped layer, the electrostatic passivation induced by the doped layer,^[24] and finally the low contact resistivity between the a-Si:H and the transparent conductive oxide (TCO) window layer, can be achieved by a single layer as shown in **Figure 1b**.

Cat-doping is essentially a post-deposition process in which silicon samples are exposed to phosphorus or boron-related radicals produced by a catalytic reaction on a heated catalyzing filament in a hot-wire chemical vapor deposition (HWCVD) system.^[25–27] The radicals can move from the filament surface and diffuse into the silicon to form a shallow doping layer. A sketch of the Cat-doping chamber used in this work is shown in **Figure S1** (Supporting Information). Former studies have shown that Cat-doping can further improve the conductivity of silicon thin films

compared to the values that is achievable for as-grown films,^[28] or improve the passivation quality of SHJ structures with treating on different interfaces.^[29,30] Primary results of applying Cat-doping on SHJ solar cells have also been demonstrated by Ohdaira et al.^[31] and Liu et al.,^[32] even though low efficiency was achieved and the limitations still need more investigation.

In this work, we have systematically investigated the phosphorus Cat-doping on a-Si:H(i) layer through a validated approach combining experiments and simulations to gain deeper insights into the Cat-doping mechanism and its beneficial application in SHJ solar cells. As shown in **Figure 1b**, the a-Si:H(i) was first deposited on the window side of the c-Si, and then converted to n-type with phosphorus Cat-doping. A certified efficiency of $23.65 \pm 0.28\%$ was demonstrated with a V_{OC} of 731.5 mV and a J_{SC} over 40.31 mA cm^{-2} , re-validating the potential of Cat-doping for SHJ solar cells. By slightly increasing the thickness of the front a-Si:H(i) layer, an improved certified efficiency of 23.76% was achieved, but the J_{SC} is compromised. The efficiency limitations for the application of Cat-doping on SHJ solar cells was analyzed and discussed. In-depth analysis of comprehensive numerical simulation reveals that the a-Si:H(i) with Cat-doping balances two levels of responsibility, providing excellent passivation and sufficient carrier selectivity. By combining two layers into one layer on the front side of SHJ solar cells, higher spectral response at short wavelengths is achieved. This cell concept also demonstrates that good passivation of c-Si directly with doped a-Si:H is possible when Cat-doping method is used.

2. Thin Film Changes with Cat-Doping

Since the phosphorus distribution in the a-Si:H(i) after Cat-doping is important for the final device performance, the phosphorus concentration profiles were characterized with time-of-flight secondary-ion mass spectrometry (SIMS) on $\approx 10 \text{ nm}$ thin films deposited on c-Si. There are several important parameters that affect the Cat-doping process, such as filament temperature, substrate temperature, and processing pressure, which have been systematically studied in our previous work.^[32] In this work, we specifically investigated the effect of Cat-doping time on the evolution of phosphorus distribution in a-Si:H(i) films. **Figure 2a** shows the phosphorus concentration (N_P) profiles in a-Si:H(i) films with different Cat-doping time and in as-deposited a-Si:H(n) layer processed by plasma enhanced chemical vapor deposition (PECVD). The doping depth is defined from the surface of the silicon thin films to the point where the phosphorus profile

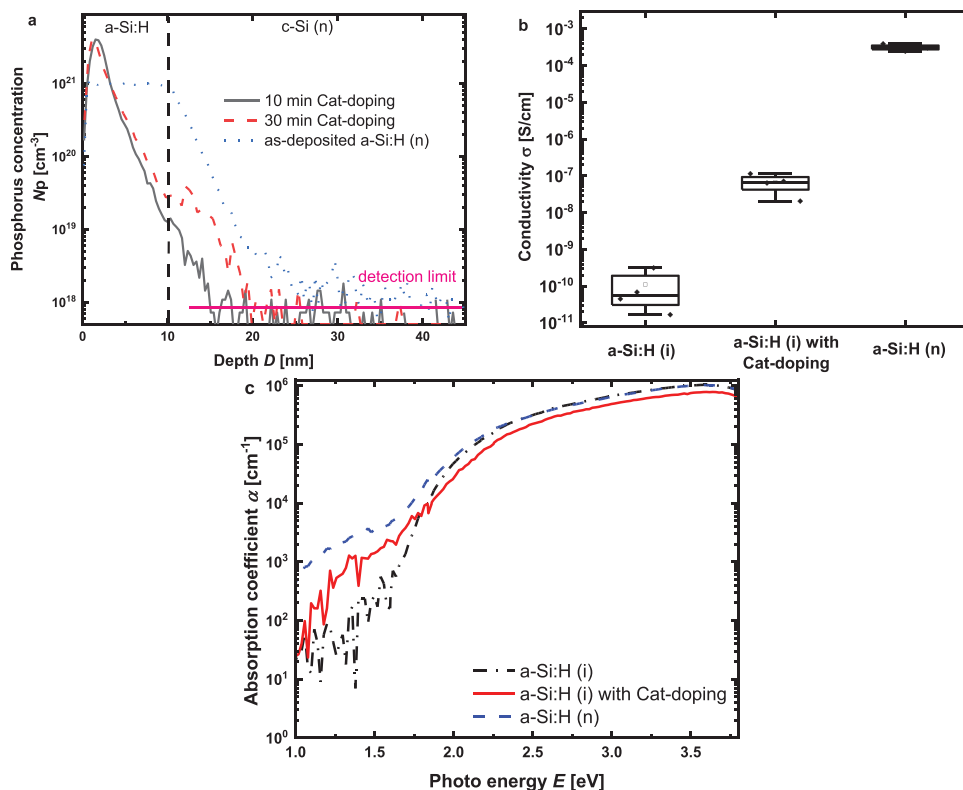


Figure 2. Electrical and optical properties of different a-Si:H layers. a) SIMS phosphorus profiles in a-Si:H(i) with 10 min Cat-doping (dark solid line), a-Si:H(i) with 30 min Cat-doping (red dash line) and as-deposited a-Si:H(n) (blue dot line). The pink solid line indicates the detection limit for SIMS. b) Box plots (minimum-maximum, 25–75%, mean: open circle symbol, median: solid line) of conductivity measurements and c), absorption coefficient measured by PDS for a-Si:H(i), a-Si:H(i) with Cat-doping and as-deposited a-Si:H(n).

reaches the detection limit of SIMS. The slope signal measured in the c-Si could be affected by the knock-on effect of the probe ions.^[33] The a-Si:H(i) samples with Cat-doping reach a very high phosphorus concentration in the first few nanometers (≈ 2 nm) below the surface, with a measured N_p of $4.0 \times 10^{21} \text{ cm}^{-3}$. Thereafter, the concentration decreases rapidly with depth, and the penetration depth of phosphorus atoms is slightly more than 10 nm. The time of Cat-doping does not seem to play a major role in the present condition; there is only slightly increase in the maximum phosphorus concentration with an N_p of more than $4.3 \times 10^{21} \text{ cm}^{-3}$ for the 30 min doping. To simplify the process, 10 min Cat-doping time is always used in the following studies. The as-deposited a-Si:H(n) sample shows a very constant phosphorus concentration through the layer with an N_p of $1.1 \times 10^{21} \text{ cm}^{-3}$. In the first few nanometers (≈ 4 nm) of the a-Si:H films, the Cat-doped layer shows a much high phosphorus concentration than the as-deposited n-type layer.

The impact of Cat-doping on the electrical properties of a-Si:H(i) films is evaluated by measuring the conductivity with evaporated silver coplanar contacts in vacuum. Since reliable conductivity requires a certain thin film thickness, a stack consisting of four times 5.5 nm a-Si:H(i) with Cat-doping was prepared (Figure S2, Supporting Information), where each deposition of 5.5 nm a-Si:H (i) is followed by the Cat-doping process. The reason for choosing 5.5 nm a-Si:H(i) is that this is the thickness used in the SHJ solar cells with Cat-doping which will be discussed

later. On the other hand, although the phosphorus can penetrate more than 5.5 nm into a-Si:H (i), the N_p is below $1 \times 10^{20} \text{ cm}^{-3}$ thereafter, which is much lower compared to the peak point. Thus, Cat-doping on the later deposited layer does not change the phosphorus distribution in the previous a-Si:H(i) layer. As shown in Figure 2b, the average conductivity of a-Si:H(i) with Cat-doping was measured to be $6.8 \times 10^{-8} \text{ S cm}^{-1}$, which is an improvement of almost three orders of magnitude over the undoped a-Si:H(i) layer. However, the average conductivity of the as-deposited a-Si:H(n) shows a much higher value of $3.1 \times 10^{-4} \text{ S cm}^{-1}$ compared to the a-Si:H (i) with Cat-doping. While the SIMS analysis can only give the total dopant concentration, the electrochemical capacitance–voltage (ECV) measurements can provide an approximation of the electrically active dopant concentration. To clarify the activation ratio of phosphorus atoms, ECV measurements were carried out on the a-Si:H(i) films with Cat-doping and on the as-deposited a-Si:H(n) films; the results are shown in Figure S3 (Supporting Information). It should be noted that ECV profiling in amorphous materials is very difficult to perform. We conducted many measurements to obtain a reliable peak value for both types of samples. Then, we assume a decay profile for the sample with Cat-doping. For the as-deposited a-Si:H(n) film, we adopted the peak value and the step function according to the depth. The maximum active dopant concentration in a-Si:H(i) with Cat-doping is found to be $2.0 \times 10^{19} \text{ atoms cm}^{-3}$, which is two orders of magnitude lower than the phosphorus

concentration measured by SIMS. This means that less than 1% of the phosphorus is activated and contributes to the electrical properties of the film with Cat-doping. In contrast, the maximum active dopant concentration in as-deposited a-Si:H(n) was measured to be 3.2×10^{20} atoms cm^{-3} . This corresponds to an activation efficiency of 29%, demonstrating the effectiveness of in situ deposition in activating phosphorus atoms. The low conductivity of a-Si:H(i) with Cat-doping is obviously due to the low activation efficiency of phosphorus atoms.

The efficiency of doping with impurities can differ by the way how the impurities have been introduced into the material. In the deposition of a-Si:H(n), the doping is done in the gas-phase by adding appropriate amounts of phosphine dopant gas. The high energy of the plasma could allow much phosphorus to be incorporated into the silicon networks and complete the bonding construction, ensuring a highly doping configuration.^[34] It is believed that a-Si:H films are mainly composed of two phases: A densely packed phase containing relatively little hydrogen, and a defect- and hydrogen-rich phase.^[35] This structure provides channels for phosphorus atoms to enter the a-Si:H(i) during the Cat-doping process. The phosphorus atoms in the dense part can be located in the interstices, which require large energies to form the Si–P bonds. The porous part has some voids, boundaries, or dangling bonds, which are sensitive to low temperature transport^[36] and may form Si–P bonds more easily and become an active doping region. Thus, the electrical properties of a-Si:H(i) with Cat-doping may be limited to the low-temperature process and affected by the microstructure of the thin films. The exact mechanism needs further investigation.

When used as a window layer, not only the electrical properties are important, but also the optical properties of a-Si:H(i) with Cat-doping should be clarified. As shown in Figure 2c, photothermal deflection spectroscopy (PDS) measurements were performed on various a-Si:H films. At lower photon energies, the absorption coefficient is highest for the as-deposited a-Si:H(n) film, which can be attributed to the increased bulk defects formation due to the dopants. The lowest defect density is found for the a-Si:H(i) layer. After Cat-doping, the defect density appears to increase but still remains significantly lower than that of the a-Si:H(n) layer. The incorporation of phosphorus atoms into the a-Si:H matrix increases the density of the atoms, thereby increasing the bandgap. This can be seen from the relative shift of the curve to higher photon energies.

3. Cat-Doping on SHJ Solar Cells

The ability of phosphorus Cat-doping and each layer deposition to passivate SHJ solar cells is shown in **Figure 3**. The minority carrier lifetime measurements were performed after each fabrication step: 1) a-Si:H depositions on both sides (PECVD precursor), 2) Cat-doping on a-Si:H(i) films when a-Si:H(n) is omitted, 3) TCO coating on both sides, and 4) post-treatment including annealing and light soaking, which mimics the post-metallization curing process for solar cells. For the reference sample with 3.5 nm a-Si:H(i) and 4.0 nm a-Si:H(n) on the window side, as shown in Figure 3a, slight degradation is observed after TCO deposition. Here, Sn-doped indium oxide (ITO) was used as TCOs on both sides of the cells. This degradation can be fully recovered after the post-treatment process. It should be noted that the

bending in the low carrier density region is not due to sputtering damage, but mainly due to the mismatch of the work functions between ITO and p-type a-Si:H (a-Si:H(p)).^[37] When the doped layer on the window side is omitted, we observed a much lower lifetime with the PECVD precursor (see Figure 3b) compared to the reference in Figure 3a. At the same time, degradation caused by ITO sputtering was also observed, which cannot be fully recovered after the post treatment. As the thickness of a-Si:H(i) increases, the surface passivation saturates with only a-Si:H(i) on the front surface at a film thickness of about 5 nm, and a minority carrier lifetime of around 1.5 ms at a charge carrier density of 1.0×10^{15} cm^{-3} is achieved. The degree of sputter-induced degradation also strongly dependent on the a-Si:H(i) thickness, as the gap between the blue dashed lines and the red dotted lines gradually decreases with increasing thickness of the a-Si:H(i), see Figure 3b–e. For 6.5 nm thick a-Si:H(i), the sputtering damage can be fully cured by post treatment. When the lifetime of the PECVD precursor is not limited by the thickness of a-Si:H(i), as shown in Figure 3c–e, the lifetime can be increased throughout the charge carrier density range after the Cat-doping process. For instance, in Figure 3d, the minority carrier lifetime is 2.4 ms with an implied V_{OC} (iV_{OC}) of 745 mV after Cat-doping, which is slightly higher than the PECVD precursor in reference sample with a lifetime of 2.0 ms and an iV_{OC} of 742 mV.

In SHJ solar cells, a-Si:H(i) with a porous interfacial layer is required to suppress epitaxial growth and ensure a high passivation quality.^[38] An optimal thickness of the a-Si:H(i) layer to ensure a good passivation is approximately the thickness at which the growth of the a-Si:H(i) layer reaches a steady state after the formation of the porous interface structure.^[39] This is the main reason for the lower minority carrier lifetime for the PECVD precursor in Figure 3b when the a-Si:H(i) layer is too thin. In Figure 3c–e, the lower lifetime of the PECVD precursors compared to the reference is due to lack of field effect passivation. As discussed in our previous work,^[40] the coexistence of thermal annealing and phosphorus doping in the Cat-doping process could lead to an improvement in chemical passivation and field effect passivation, respectively. Since the thickness of the a-Si:H(i) layer used in the passivation structure is thinner than the penetration depth of the P atoms, a shallow doped region should form on the surface of the c-Si substrate, which could also act as a front surface field and improve the passivation.^[24] This important aspect will be particularly discussed in the following section. During ITO sputtering, the energetic particles generated by the sputtered atoms, reflected neutrals and ions with energies up to the target voltage multiplied by the elementary charge can penetrate through a-Si:H layer and create defects at the a-Si:H/c-Si interface, leading to passivation deterioration.^[41] The silicon-hydrogen configuration of the a-Si:H(i) thin film can be permanently altered if too much energy is introduced, and the passivation cannot be restored after post-treatment.^[42] As the a-Si:H(i) film thickness increases, a smaller number of harmful particles are expected to reach near the a-Si:H/c-Si interface, and the degradation in lifetime caused by sputtering is reduced. This explains the trend before and after ITO deposition in Figure 3b–e.

As mentioned earlier, a certain thickness of a-Si:H(i) is mandatory to keep good passivation, which is required to achieve high V_{OC} and pseudo-FF (pFF) in SHJ solar cells. However, a greater thickness of the a-Si:H(i) film also leads to higher parasitic

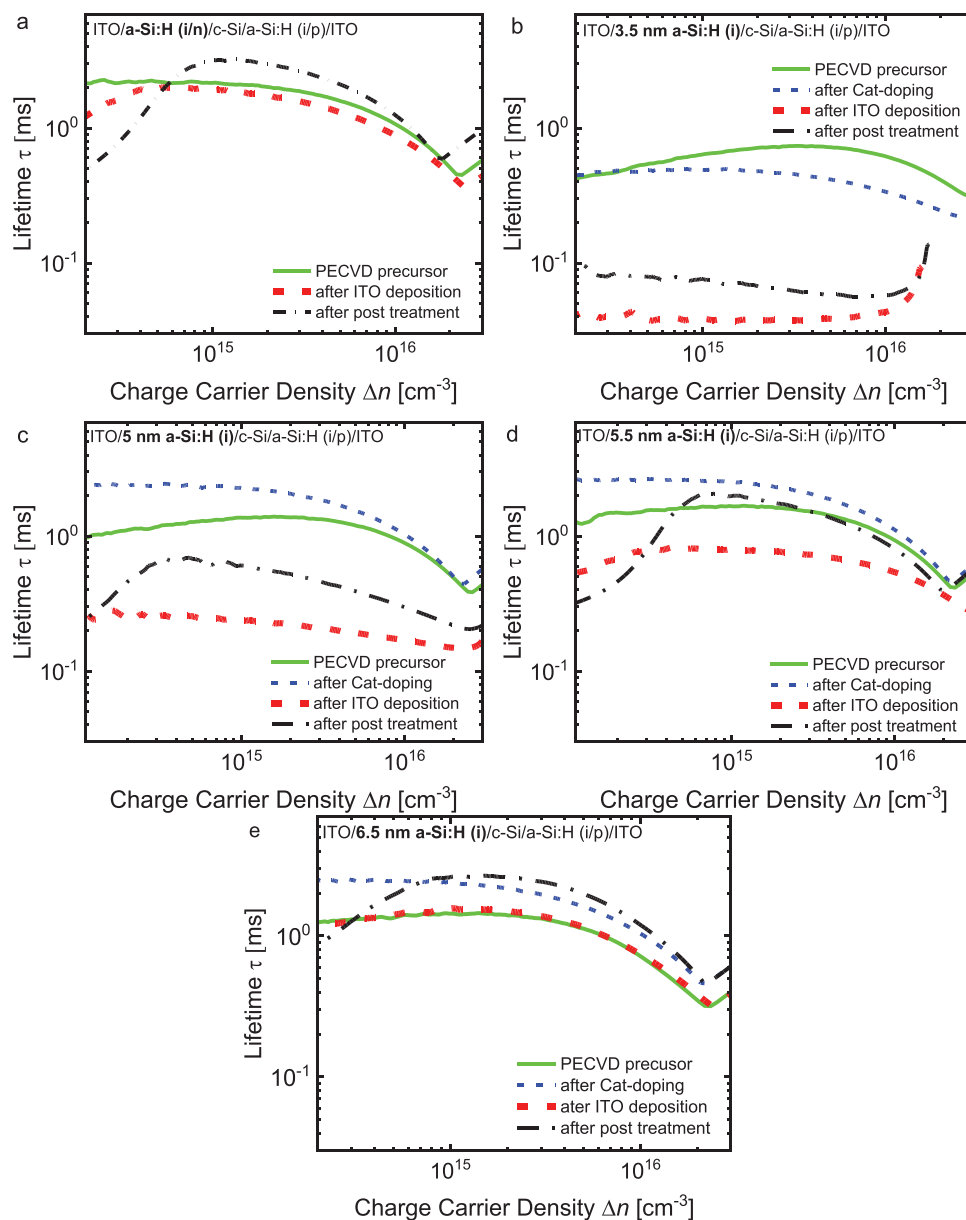


Figure 3. Information of minority carrier lifetime evolution for different samples after different process. These are lifetimes for a) reference SHJ sample with a-Si:H(i/n) stack, b) 3.5 nm a-Si:H(i) with Cat-doping, c), 5.0 nm a-Si:H(i) with Cat-doping, d), 5.5 nm a-Si:H(i) with Cat-doping and e) 6.5 nm a-Si:H(i) with Cat-doping after prepared from PECVD system, Cat-doping, ITO deposition on both side and post treatment. All the samples have the same a-Si:H(i/p) stack on the rear side after PECVD process.

absorption and thus lower J_{SC} . A careful compromise between these parameters must be made in cell fabrication. First, we fabricated SHJ solar cells with Cat-doping on 5.5 nm a-Si:H(i) for comparison with a-Si:H(i/n) reference cells. The reason for choosing this layer thickness is the relatively low sputter-induced passivation degradation and the thinner thickness compared to the reference cell, which has a total a-Si:H layer stack of 7.5 nm. **Figure 4** summarizes the in house measured $J-V$ parameters of SHJ solar cells with a-Si:H(i/n), a-Si:H(i), and a-Si:H(i) with Cat-doping as window layers. It can be seen that the cells with only one a-Si:H(i) layer have much worse parameters compared to the other groups. Since the a-Si:H layer is not doped, the solar cells have no field ef-

fect passivation, which leads to very low V_{OC} and FF values. The cells with Cat-doping on a-Si:H(i) exhibit a decent efficiency of over 23%, as shown in Figure 4a. This demonstrates the capability of applying Cat-doping on SHJ solar cells, where the Cat-doped a-Si:H(i) can provide sufficient carrier selectivity and prevent excessive carrier recombination. The J_{SC} values of the Cat-doped solar cells shown in Figure 4c are quite high compared to the a-Si:H(i/n) reference cells. The J_{SC} gain is due to lower parasitic absorption by using a thinner a-Si:H window layer. This is confirmed by the higher external quantum efficiency (EQE) in the short wavelength region, as shown by the arrow in Figure S4 (Supporting Information). In contrast, the average V_{OC} of the

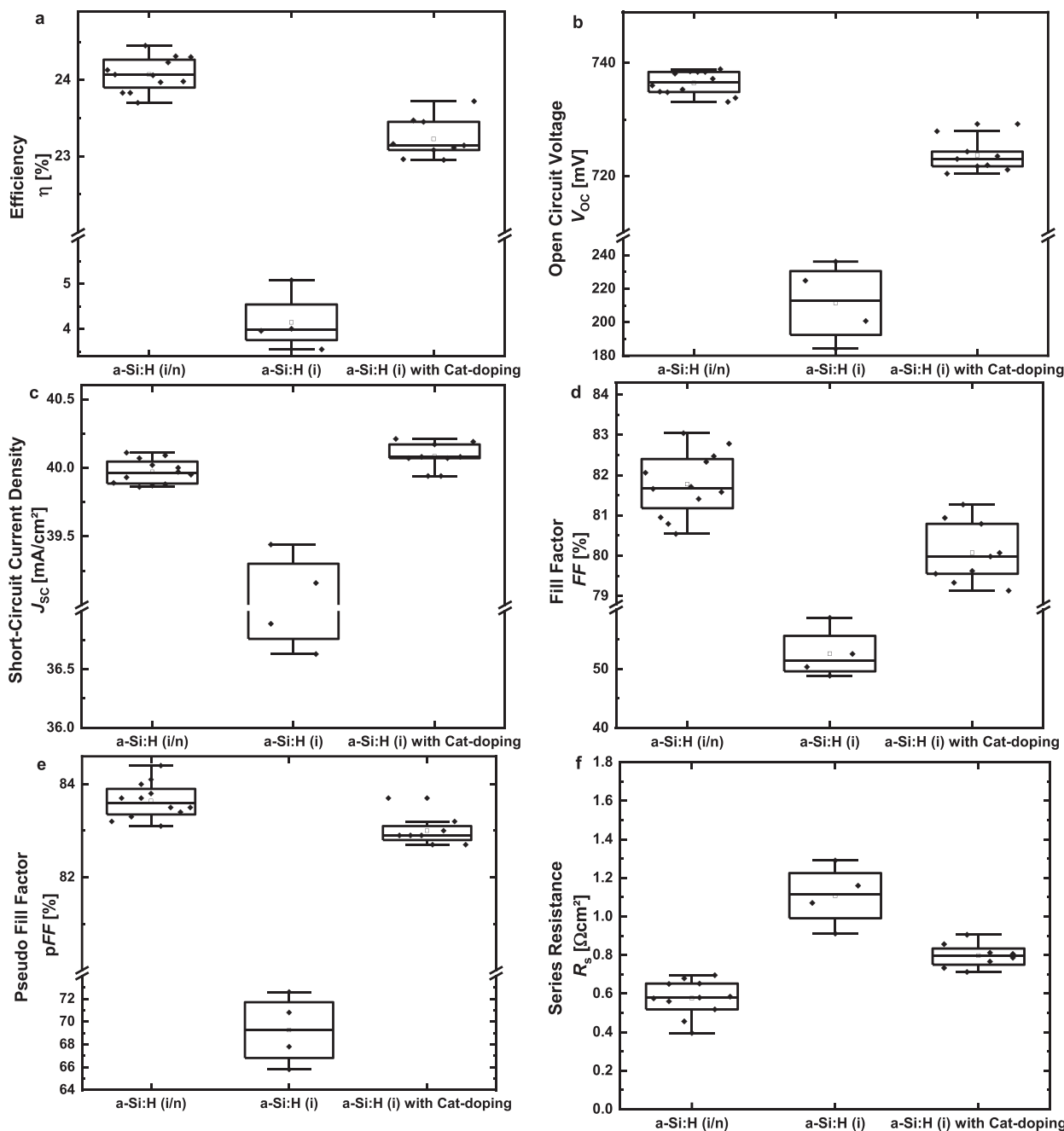


Figure 4. Comparison of J - V performances of SHJ solar cells fabricated with a-Si:H (i/n), a-Si:H (i) and a-Si:H (i) with Cat-doping as window layers. Box plots (minimum-maximum, 25–75%, mean: open circle symbol, median: solid line) shows the a) efficiency η , b) open-circuit voltage V_{OC} , c) short-circuit current density J_{sc} , d) fill factor FF , e) pseudo fill factor pFF , and e) series resistance R_s measured in house.

solar cells with Cat-doping is about 8 mV lower than that of the reference cells, as shown in Figure 4b. This V_{OC} limit is primarily due to passivation degradation caused by sputtering, which is consistent with the previous discussion on lifetime. This is also reflected in the lower pFF , as displayed in Figure 4e. Another noticeable piece of information in Figure 4f is that the solar cells with Cat-doping have a higher series resistance (R_s) than the reference cells. To investigate the reason for the R_s difference, measurements were made using the transmission line method

(TLM) to determine the contact resistivity in the front stack. As shown in Figure S5 (Supporting Information), the average front contact resistivity in stacks with Cat-doping is $0.32 \Omega \text{ cm}^2$, which is much higher compared to the a-Si:H(i/n) reference sample with an average value of $0.12 \Omega \text{ cm}^2$. This is mainly due to the higher contact resistivity between the a-Si:H(i) with Cat-doping and ITO. Thus, the lower FF in the solar cells with Cat-doping can be attributed to two factors: the unrecoverable sputter-induced passivation degradation and higher contact resistivity in the

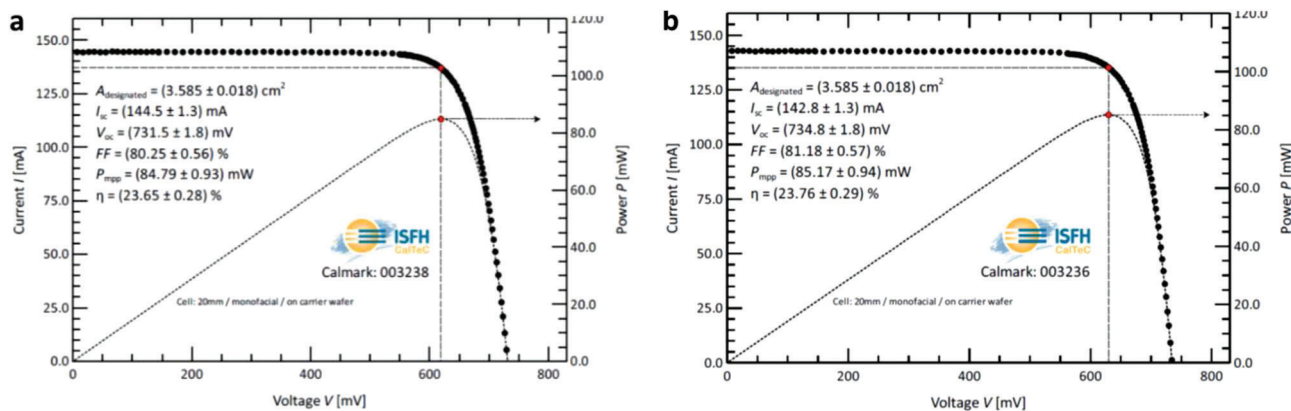


Figure 5. IV results of the certified SHJ solar with Cat-doping. a) Cat-doping on 5.5 nm a-Si:H(i) and b) Cat-doping on 6.5 nm a-Si:H(i) were used on the front side of the solar cells.

window layers. Overall, the J_{SC} in SHJ solar cells with Cat-doping has increased obviously, however, the efficiency is currently limited by the relatively lower V_{OC} and FF in our case. In order to address these issues, one can work from two aspects. First, soft TCO deposition on thin a-Si:H(i) with Cat-doped layer needs to be carefully investigated to improve the V_{OC} and FF . Besides, further optimization of Cat-doping process or modification of the microstructure of a-Si:H(i) may help active more dopants in the layer with Cat-doping, in order to reduce to contact resistance with the following TCO.

An MgF_2 layer was then used as a double antireflection coating to reduce the reflectivity, and an Ag back reflector was sputtered on to increase the rear reflection of the best solar cell in the series with Cat-doping on 5.5 nm a-Si:H(i). The performance of this cell was independently certified by CalTeC at the Institute for Solar Energy Research in Hamelin as shown in **Figure 5a**. An efficiency of 23.65% and a high J_{SC} of 40.31 mA cm^{-2} were demonstrated, proving the potential of using Cat-doping to enhance the current generation in high-efficiency SHJ solar cells. In addition, a solar cell with Cat-doping of 6.5 nm a-Si:H(i) was fabricated and certified, as shown in **Figure 5b**. The use of a thicker a-Si:H(i) layer results in an improved efficiency to 23.76% due to increased V_{OC} and FF , but a reduced J_{SC} of 39.83 mA cm^{-2} . The evolution of solar cell parameters suggests again the importance of soft TCO deposition on thin a-Si:H(i) with Cat-doping.

4. Proof-of-Concept with Simulation

To investigate how Cat-doping works for SHJ solar cells even at very low active dopant concentration, we use the Sentaurus Technology Computer Aided Design (TCAD) device simulation tool to model the solar cells. **Figure 6** shows the cell performance parameters as a function of the active carrier concentration of doped a-Si:H window layers in SHJ solar cells with Cat-doping on a-Si:H(i), a-Si:H(n), and a-Si:H(i/n), respectively. The detailed device information of the three cell configurations can be found in **Figure S6** (Supporting Information). **Figure 6a** shows that the SHJ solar cells with Cat-doping can keep a high V_{OC} value as long as the active carrier concentration is higher than $2 \times 10^{19} \text{ cm}^{-3}$. However, the reference cell with a-Si:H(i/n) requires a carrier concentration higher than $1 \times 10^{20} \text{ cm}^{-3}$ to maintain a stable V_{OC} .

In the solar cell with only as-deposited a-Si:H(n), due to the absence of a-Si:H(i), an even higher active carrier concentration in the a-Si:H(n) is required for good surface passivation to obtain a sufficiently high V_{OC} . The evolution for FF and J_{SC} displayed in **Figure 6b,c** shows a similar trend as for the V_{OC} . In the a-Si:H(i/n) reference solar cell, the underlying a-Si:H(i) can provide very good surface chemical passivation, but when electrons pass through the highly defective as-deposited a-Si:H(n), a high active carrier concentration is required to achieve sufficient field effect passivation for successful collection by the subsequent ITO layers. In contrast, in the SHJ solar cell with Cat-doping, the material defect density of the a-Si:H(i) is relatively low, so the carriers are not recombined as easily and thus there is less requirement for field effect passivation. Moreover, the penetration of phosphorus atoms through thin a-Si:H(i) onto the c-Si surface also plays an important role here. Here we have considered the same phosphorus diffusion in c-Si as in a-Si:H(i). The comparison of the band diagrams of the three cell configurations at a working voltage of 600 mV is plotted in **Figure 7**. It shows that an order of magnitude lower peak active carrier concentration in the Cat-doping profile results in comparable band bending in the wafer toward the interface as in the a-Si:H(i/n) and a-Si:H(n) samples. This is also confirmed by an independent surface photovoltage (SPV) measurement, where the a-Si:H(i) with Cat-doping exhibits similar band bending to the c-Si as the as-deposited a-Si:H(n) layer. Further details can be found in **Figure S7** and **Table S1** (Supporting Information). The doping impurity in the c-Si surface can lead to the formation of band bending, which prevents minority hole carriers from reaching the a-Si:H/c-Si interface. This is beneficial for field effect passivation and carrier selectivity. Compared to the other two types of solar cells, a higher potential barrier is observed between a-Si:H(i) with Cat-doping and ITO, which is due to the low carrier activation in Cat-doped a-Si:H(i) layer. This is responsible for the higher R_s in the Cat-doped SHJ solar cell, as shown in the last section.

As the active carrier concentration decreases, the carrier selectivity deteriorates and lead to a significant decrease in J_{SC} and V_{OC} as already shown in **Figure 6**. However, the V_{OC} suddenly goes up when the active carrier concentration is very low, as shown in **Figure 6a**. To explain this, the band diagrams at different active carrier concentrations of the three cell configurations are given

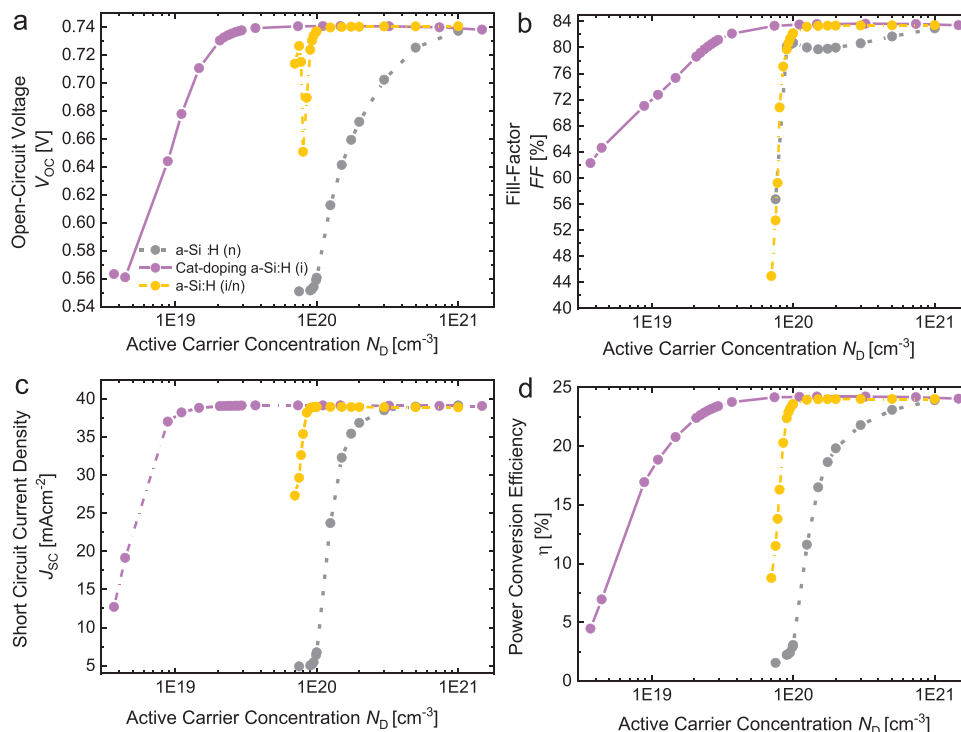


Figure 6. Simulated cell performance parameters versus active carrier concentration of carrier-selective a-Si:H window layers in SHJ solar cells with Cat-doping on a-Si:H(i), a-Si:H(n), and a-Si:H(i/n), respectively. For reasonable comparison of the three configurations, thickness of 5.5 nm a-Si:H (i) in the solar cell with Cat-doping, 5.5 nm a-Si:H(n) in the cell without a-Si:H(i) and 3.5 nm a-Si:H(i)/4.0 nm a-Si:H(n) in the reference cell were used. For the Cat-doped solar cell, N_D represents the peak value of $N_D(\lambda)$ which has the same profile shape as in Figure S3a (Supporting Information).

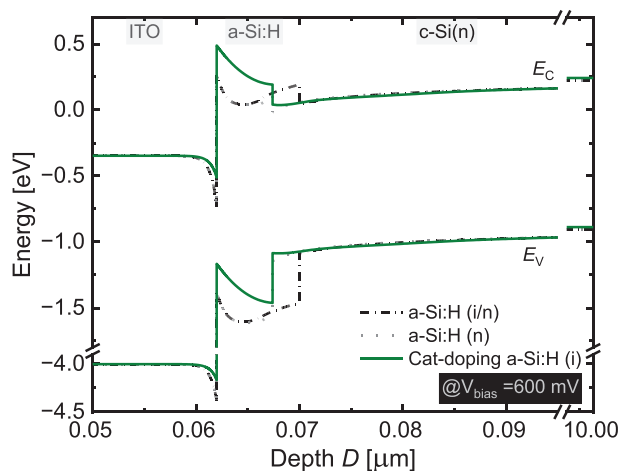


Figure 7. Band diagram comparison of SHJ solar cells with Cat-doping on a-Si:H(i), a-Si:H(n) and a-Si:H(i/n) in the front side. The profiles were plotted at a working voltage of 600 mV for all the cells.

in Figure S8 (Supporting Information). Below a certain value of active carrier concentration, a reverse band bending is observed, leading to a potential barrier for electrons near the interface. As a result, the charge carriers are confined to the bulk region, and recombination at the interface is suppressed. This will increase the total free carrier lifetime. Therefore, a jump in V_{OC} can be observed at very low active dopant concentration, as shown in

Figure 6a at the lowest N_D for the a-Si:H(i/n) reference cell. Even though the shape of the band structure varies for different cell types, all SHJ configurations show this effect. From the band diagram of the solar cell with Cat-doping in Figure S8a (Supporting Information), the bandgap of c-Si narrows significantly near the interface at an extremely high active carrier concentration. This is the result of Cat-doping on the c-Si surface after penetration of the thin a-Si:H(i) layer. At extremely high activation, the expansion of charge carriers onto the wafer is so high that there is a significant narrowing of the effective bandgap, which can be seen from the difference between the conduction and valence band energy. The Bennett–Wilson bandgap narrowing model implemented in Sentaurus TCAD is used for these simulations.^[43]

5. Conclusion

The present work has demonstrated the potential of using a-Si:H(i) with Cat-doping as window layer in SHJ rear junction solar cells to reduce the parasitic absorption of the silicon thin films. A single a-Si:H(i) passivation layer with Cat-doping provides the functionalities in terms of passivation and carrier selectivity that otherwise would require an a-Si:H(i)/a-Si:H(n) bilayer stack with higher parasitic absorption. It is found that even though lots of phosphorus atoms can be incorporated into the a-Si:H(i) during the Cat-doping process, the dopant activation is too low to improve its conductivity significantly. Besides, Cat-doping on a-Si:H(i) improves the passivation quality by introducing field effect passivation in the structure. However, the TCO sputter

damage needs to be carefully considered here especially when thinner window layer is used. Finally, a J_{SC} of 40.31 mA cm⁻² and efficiencies exceeding 23.6% have been preliminary demonstrated. There are two aspects that need to be further investigated to improve the efficiency of the solar cell with Cat-doping, namely, developing soft TCO sputtering on thinner a-Si:H(i) layers for higher V_{OC} and how to get higher dopant activation in the a-Si:H(i) with Cat-doping to reduce the contact resistivity with TCO. Numerical simulations using Sentaurus TCAD show that SHJ solar cells with Cat-doping have much lower active carrier concentration requirement for sufficient field effect passivation and carrier selectivity compared to the traditional SHJ reference solar cells. This is mainly due to the lower defect density in the a-Si:H(i) even with post doping. In addition, the penetration of phosphorus through the thin a-Si:H(i) into the c-Si surface could lead to increased doping impurity and cause the formation of downward band bending, which is beneficial for field effect passivation. The combination of the above experimental and simulation discussions provides a comprehensive understanding of applying Cat-doping in SHJ solar cells that shows current limitations that needs to be addressed in future research work.

6. Experimental Section

Cat-Doping Process: Cat-doping was performed in a HWCVD chamber with three curved tantalum filaments arranged parallel to each other. The samples were placed face-down 90 mm above the filaments. The heater temperature was set at 200 °C. To achieve a stable temperature on the substrates, hydrogen gas was allowed to enter the chamber for 10 min while the pressure in the chamber was maintained at 0.5 mbar. After pre-heating, the hydrogen gas was pumped out of the chamber and Cat-doping could be initiated. A gas consisting of 2% phosphine in helium was introduced into the chamber at a flow rate of 20 sccm while the pressure in the chamber remained constant at 0.01 mbar. The filament temperature was set at 2200 °C.

Fabrication of Passivation Samples and Solar Cells: The passivation samples and solar cells were fabricated using Czochralski grown n-type as-cut <100> wafers from LONGi with a thickness of 160 μm and resistivity of around 1 Ω cm. First, the wafers were removed from saw damage and textured in alkaline solution to form surface pyramids. Then, the wafers were cleaned with an ozone process followed by native oxide removal in 1% diluted hydrofluoric acid for 5 min. The a-Si:H layers were deposited in a Meyer Burger AK1000 PECVD system. Different thickness of a-Si:H(i) layers and 3.5 nm a-Si:H(i)/4.0 nm a-Si:H(n) were deposited on the front surface of the Cat-doped samples and the reference samples, respectively. Afterward, 6 nm a-Si:H(i) and 13 nm a-Si:H(p) layers were sequentially deposited in two chambers. Subsequently, Cat-doping process was applied to the a-Si:H(i) layers for Cat-doped samples. About 70 nm ITO layers were sputtered on both sides of the samples from a 3% doped rotary target at a sample heater temperature of 250 °C. For passivation samples, the ITO layers were sputtered on the entire surface of the substrates. For solar cells, the ITO layers were fabricated by masking to create four 2 × 2 cm² solar cell pieces on each wafer. The Ag grids (width of ≈60 μm) with busbars on the edge of the cells were screen printed on an MT-650TVC screen printer from Microtec using a low-temperature silver paste. They were then dried at 150 °C for 10 min and cured at 170 °C for 40 min. Heat-assisted light soaking treatment was then performed in a Gsola system with a heater temperature of 175 °C under 20 suns for 90 s. A 110 nm thick MgF₂ double antireflection coating layer was thermally evaporated on the front side of the best solar cells using an electron beam, followed by sputtering of a 200 nm thick Ag back reflector. The photographs of the actual device are shown in Figure S10 (Supporting Information).

Material Characterization: The main objective of the SIMS measurement was to determine the phosphorus concentration in the Cat-doped a-Si:H(i) on the c-Si wafer substrate. The SIMS measurements were performed using a ToF-SIMS-5-NCS from IONTOF GmbH. The surface of the samples is bombarded with a primary ion beam of Cs⁺ with an energy of 1 keV. A collision cascade is induced by this bombardment and secondary ions are generated from the sample. These secondary ions are accelerated by an electric field and their time of flight from the surface to the detector is determined and depends on the mass/charge ratio. Due to the high detection accuracy, the mass resolution of the SIMS measurement is extremely high.^[44] When the secondary ions leave the sample, a crater is formed in which the primary ion beam continues to sputter secondary ions. This leads to a good depth resolution.

The concentration of active phosphorus doping of Cat-doped a-Si:H(i) was measured by ECV. The measurements were conducted with a Wafer Profiler CVP21 from WEP. During the measurement, the Cat-doped a-Si:H(i) film was pressed against a sealing ring, which determined the contact area A. Through this ring, the electrolyte (0.1 M NH₄HF₂) was brought into contact with the Cat-doped a-Si:H(i) layer. During etching, a Schottky contact was formed, creating a depletion zone in which no charge carriers were present. This depletion zone contained ionized donors and electrically active defects, that acted like a capacitor. The capacitance C was measured. Therefore, the active doping concentration (N_D) can be obtained with:

$$N_D = \frac{1}{qA^2\epsilon_r\epsilon_0} \frac{C^3}{dC/dV} \quad (1)$$

where q is the elementary charge, ϵ_r is the relative permittivity of the Cat-doped a-Si:H(i), ϵ_0 is the vacuum permittivity, and V is the voltage. After each capacitance measurement, the surface of the semiconductor was electrolytically etched to obtain a depth profile of the carrier concentration. The profiling depth was the sum of the etch depth and the depletion width since the active carrier concentration was measured at the end of the depletion zone. The etch depth is obtained using Faraday's law and the depletion width (X_{dep}) is determined with^[45]:

$$X_{dep} = \frac{\epsilon_0\epsilon_r A}{C} \quad (2)$$

Passivation Characterization: The passivation quality of the layers was characterized by measuring the photo-conductance of the samples using a Sinton WCT-120 lifetime tester. From these measurements, the iV_{OC} on one sun and the effective minority charge carrier lifetime at an excess carrier density of 1×10^{15} cm⁻³ were extracted.

Device Characterization: Contact resistivity was measured on an in-house setup using the TLM. The contact resistivity was evaluated for the complete front side layer stack of c-Si/Cat-doped a-Si:H(i) or a-Si:H(i/n)/ITO/Ag. Parameters related to solar cell performance were measured by IV measurements under standard test condition (AM1.5 g, 25 °C and 100 mW cm⁻²) using the LOANA solar cell analysis system from pv-tools with a Wavelabs Sinus 220 light sources. The EQE was also measured with the LOANA system.

Simulation Procedures: The opto-electrical device simulation model used in this work is based on Sentaurus TCAD.^[46] A virtual representation of the physical device was created based on a finite-element mesh. It was then used to numerically solve the physical equations governing the optical and electrical properties of the device. The device simulation was decoupled into an optical and an electrical part. The optical response of the solar cell was simulated using raytracing in the thick c-Si layer, coupled with transfer matrix method for the thin contact films. For this purpose, the optical properties of the materials involved were taken from spectroscopic ellipsometry measurements. The optical generation profile resulting from the optical simulation was then used for the subsequent electrical simulation. To model the charge carrier transport via band-to-band tunneling at the doped a-Si:H/ITO contact, a non-local tunneling model as implemented in Sentaurus TCAD was used in the 2D electrical device simulation. Furthermore, a contribution of trap-assisted tunneling via traps in

a-Si:H layers was included. The basic input parameters for the electrical model are listed in Table S2 (Supporting Information). The distributions of trap states in the a-Si:H layers and interfaces used in this work are adapted from the literature and are listed in Table S3 (Supporting Information). The device model has been validated to agree with the certified efficiency of 24.5% on a mono facial SHJ solar cell.^[35]

Three types of SHJ solar cells were simulated to investigate the effect of active carrier concentration on the cell performance, including the solar cells with Cat-doping on a-Si:H(i), solar cells with only a-Si:H(n) and solar cells with a-Si:H(i/n). Comparable V_{OC} values were estimated for an interface defect density of 3×10^{11} for cells with a-Si:H(i/n) and $1 \times 10^{13} \text{ eV}^{-1} \text{ cm}^{-2}$ for cells with a-Si:H(n), with active carrier concentration $N_D = 2 \times 10^{20} \text{ cm}^{-3}$ of a-Si:H(n) layer. For solar cell with Cat-doping on a-Si:H(i), the defect density of $5 \times 10^{10} \text{ eV}^{-1} \text{ cm}^{-2}$ gave a good approximation to the cell V_{OC} and FF with the measured active carrier concentration profile $N_D^{\text{cat-dop}}(\zeta)$ as the ECV profile shown in Figure S3a (Supporting Information). In Figure 6a (Supporting Information), the active carrier concentration of Cat-doping sample represents the peak value of $kN_D^{\text{cat-dop}}(\zeta)$ profile, where k is a weighting value and ζ is depth. The input profile shape of active carrier concentration for Cat-doping sample was always kept identical, except weighted with certain values of k , as shown in Figure S9 (Supporting Information).

Supporting Information

Supporting Information is available from the Wiley Online Library or from the author.

Acknowledgements

The authors would like to thank the support from Alain Doumit for the wafer texture and cleaning, Siekmann for the ITO sputtering, and Silke Lynen for the screen printing. This work was supported by the Helmholtz Energy Materials Foundry (HEMF) infrastructure funded by the Helmholtz Association.

Open access funding enabled and organized by Projekt DEAL.

Conflict of Interest

The authors declare no conflict of interest.

Author Contributions

W.D. and K.D. conceived the project. W.D. and G.M. designed all the experiments. G.M. conducted the device and thin film characterization. H.T.G., K.B., and W.D. carried out the device simulation. A.L., V.L., M.A.Y., K.Z., and Q.Y. organized and fabricated the SHJ solar cells and thin film samples. B.X. and A.E. fabricated the back reflector and the double antireflective coating. N.N. and L.K. conducted the SPV measurement. W.D., K.D., and U.R. supervised the research. W.D. wrote the manuscript. All authors were involved in the discussion of the results.

Data Availability Statement

The data that support the findings of this study are available on request from the corresponding author. The data are not publicly available due to privacy or ethical restrictions.

Keywords

Cat-doping, carrier selectivity, silicon heterojunction, transparency

Received: September 10, 2023

Published online:

- [1] <https://taiyangnews.info/business/global-cumulative-pv-capacity-exceeds-1-tw/>.
- [2] N. M. Haegel, P. Verlinden, M. Victoria, P. Altermatt, H. Atwater, T. Barnes, C. Breyer, C. Case, S. De Wolf, C. Deline, M. Dharmrin, B. Dimmler, M. Gloeckler, J. C. Goldschmidt, B. Hallam, S. Haussener, B. Holder, U. Jaeger, A. Jaeger-Waldau, I. Kaizuka, H. Kikusato, B. Kroposki, S. Kurtz, K. Matsubara, S. Nowak, K. Ogimoto, C. Peter, I. M. Peters, S. Philipps, M. Powalla, et al., *Science* **2023**, *380*, 39.
- [3] M. Taguchi, *ECS J. Solid State Sci. Technol.* **2021**, *10*, 025002.
- [4] H. Lin, M. Yang, X. Ru, G. Wang, S. Yin, F. Peng, C. Hong, M. Qu, J. Lu, L. Fang, C. Han, P. Procel, O. Isabella, P. Gao, Z. Li, X. Xu, *Nat. Energy* **2023**, *8*, 789.
- [5] M. Taguchi, A. Yano, S. Tohoda, K. Matsuyama, Y. Nakamura, T. Nishiwaki, K. Fujita, E. Maruyama, *IEEE J. Photovoltaics* **2014**, *4*, 96.
- [6] T. Mishima, M. Taguchi, H. Sakata, E. Maruyama, *Sol. Energy Mater. Sol. Cells* **2011**, *95*, 18.
- [7] T. Ruan, M. Qu, J. Wang, Y. He, X. Xu, C. Yu, Y. Zhanag, H. Yan, *J. Mater. Sci.: Mater. Electron* **2019**, *30*, 13330.
- [8] K. Okuda, H. Okamoto, Y. Hamakawa, *Jpn. J. Appl. Phys.* **1983**, *22*, L605.
- [9] H. Mimura, Y. Hatanaka, *J. Appl. Phys.* **1987**, *61*, 2575.
- [10] M. Schmidt, L. Korte, A. Laades, R. Stangl, C.h. Schubert, H. Angermann, E. Conrad, K. V. Maydell, *Thin Solid Films* **2007**, *515*, 7475.
- [11] K. V. Maydell, E. Conrad, M. Schmidt, *Prog. Photovoltaics* **2006**, *14*, 289.
- [12] R. A. Street, *Hydrogenated Amorphous Silicon*, Cambridge University Press, New York, United States of America, **1991**.
- [13] S. Noguchi, A. Noguchi, N. Murakami, US005401336A, **1993**.
- [14] J. Melskens, *Hydrogenated amorphous silicon: Nanostructure and defects*, PhD thesis, Delft University of Technology, The Netherlands, **2015**.
- [15] M. Kondo, S. De Wolf, H. Fujiwara, *Mater. Res. Soc. Symp. Proc.* **2008**, *1066*, A03.
- [16] W. Duan, K. Bittkau, A. Lambertz, K. Qiu, Z. Yao, P. Steuter, D. Qiu, U. Rau, K. Ding, *Sol. RRL* **2021**, *5*, 2000576.
- [17] K. Yoshikawa, H. Kawasaki, W. Yoshida, T. Irie, K. Konishi, K. Nakano, T. Uto, D. Adachi, M. Kanematsu, H. Uzu, K. Yamamoto, *Nat. Energy* **2017**, *2*, 17032.
- [18] K. Masuko, M. Shigematsu, T. Hashiguchi, D. Fujishima, M. Kai, N. Yoshimura, T. Yamaguchi, Y. Ichihashi, T. Mishima, N. Matsubara, T. Yamanishi, T. Takahama, M. Taguchi, E. Maruyama, S. Okamoto, *IEEE J. Photovoltaics* **2014**, *4*, 1433.
- [19] D. Qiu, W. Duan, A. Lambertz, K. Bittkau, P. Steuter, Y. Liu, A. Gad, M. Pomaska, U. Rau, K. Ding, *Sol. Energy Mater. Sol. Cells* **2020**, *209*, 110471.
- [20] Y. Zhao, L. Mazzarella, P. Procel, C. Han, G. Yang, A. Weeber, M. Zeman, O. Isabella, *Prog. Photovoltaics* **2020**, *28*, 425.
- [21] S. Kirner, L. Mazzarella, L. Korte, B. Stannowski, B. Rech, R. Schlatmann, *IEEE J. Photovoltaics* **2015**, *5*, 1601.
- [22] M. Köhler, M. Pomaska, P. Procel, R. Santbergen, A. Zamchiy, B. Macco, A. Lambertz, W. Duan, P. Cao, B. Klingebiel, S. Li, A. Eberst, M. Luysberg, K. Qiu, O. Isabella, F. Finger, T. Kirchartz, U. Rau, K. Ding, *Nat. Energy* **2021**, *6*, 529.
- [23] M. Pomaska, M. Koehler, P. Moya, A. Zamchiy, A. Singh, D. Kim, O. Isabella, M. Zeman, S. Li, K. Qiu, A. Eberst, V. Simrnov, F. Finger, U. Rau, K. Ding, *Prog. Photovoltaics* **2020**, *28*, 321.
- [24] U. Rau, T. Kirchartz, *Adv. Mater. Interfaces* **2019**, *6*, 1900252.
- [25] H. Matsumura, T. Hayakawa, T. Ohta, Y. Nakashima, M. Miyamoto, T. C. Thi, K. Koyama, K. Ohdaira, *J. Appl. Phys.* **2014**, *116*, 114502.
- [26] H. Umemoto, Y. Nishihara, T. Ishikawa, S. Yamamoto, *Jpn. J. Appl. Phys.* **2012**, *51*, 086501.
- [27] J. Seto, K. Ohdaira, H. Matsumura, *Jpn. J. Appl. Phys.* **2016**, *55*, 04ES05.

- [28] Y. Liu, D. Y. Kim, A. Lambertz, K. Ding, *Thin Solid Films* **2017**, 635, 63.
- [29] H. Matsumura, M. Miyamoto, K. Koyama, K. Ohdaira, *Sol. Energy Mater. Sol. Cells* **2011**, 95, 797.
- [30] S. Tsuzaki, K. Ohdaira, T. Oikawa, K. Koyama, H. Matsumura, *Jpn. J. Appl. Phys.* **2015**, 54, 072301.
- [31] K. Ohdaira, J. Seto, H. Matsumura, *Jpn. J. Appl. Phys.* **2017**, 56, 08MB06.
- [32] Y. Liu, M. Pomaska, W. Duan, D. Qiu, S. Li, A. Lambertz, A. Gad, U. Breuer, F. Finger, U. Rau, K. Ding, *ACS Appl. Mater. Interfaces* **2020**, 12, 56615.
- [33] E. Zinner, *Scanning* **1980**, 3, 57.
- [34] W. E. Spear, P. G. Le Comber, *Solid State Commun.* **1975**, 17, 1193.
- [35] W. Duan, A. Lambertz, K. Bittkau, D. Qiu, K. Qiu, U. Rau, K. Ding, *Prog. Photovoltaics* **2022**, 30, 384.
- [36] D. A. Anderson, W. Paul, *Philos. Mag. B* **1981**, 44, 187.
- [37] M. Bivour, C. Reichel, M. Hermle, S. W. Glunz, *Sol. Energy Mater. Sol. Cells* **2012**, 106, 11.
- [38] W. Liu, L. Zhang, R. Chen, F. Meng, W. Guo, J. Bao, Z. Liu, *J. Appl. Phys.* **2016**, 120, 175301.
- [39] H. Fujiwara, M. Kondo, *J. Appl. Phys.* **2007**, 101, 054516.
- [40] Y. Liu, M. Pomaska, W. Duan, D. Y. Kim, M. Köhler, U. Breuer, K. Ding, *Adv. Eng. Mater.* **2020**, 22, 1900613.
- [41] L. Tutsch, M. Bivour, W. Wolke, M. Hermle, J. Rentsch, *Influence of the Transparent Electrode Sputtering Process on the Interface Passivation Quality of Silicon Heterojunction Solar Cells*, 33rd published by Fraunhofer-Institut für Solare Energiesysteme EUPVSEC, Amsterdam, The Netherlands September **2017**, 29.
- [42] B. Demareux, J. P. Seif, S. Smit, B. Maccio, W. M. M. Kessels, J. Geissbuhler, S. De Wolf, C. Ballif, *IEEE J. Photovoltaics* **2014**, 4, 1387.
- [43] H. S. Bennett, C. L. Wilson, *J. Appl. Phys.* **1984**, 55, 3582.
- [44] IONTOF. <https://www.iontof.com/>.
- [45] E. Peiner, A. Schlachetzki, D. Krüger, *J. Electrochem. Soc.* **1995**, 142, 576.
- [46] Sentaurus Device User Guide, Synopsys, Inc., Mountain View, **2015**, CA, USA.